

Electronic Supplementary Information

**Iron oxide@mesoporous carbon architectures derived from
an Fe(II)-based metal organic framework for highly
sensitive oxytetracycline determination**

Yingpan Song^a, Fenghe Duan^a, Shuai Zhang^b, Jia-Yue Tian^a, Zhihong Zhang^{*a}, Zhuo-Wei Wang^a,
Chun-Sen Liu^{*a}, Wen-Ming Xu^a, Miao Du^{*a}

^a Henan Provincial Key Laboratory of Surface & Interface Science, Zhengzhou University of
Light Industry, Zhengzhou 450002, China

^b Department of Polymer Science & Materials, Faculty of Chemical, Environmental and
Biological Science and Technology, Dalian University of Technology, Dalian 116024, P. R. China

Corresponding authors:

Tel.: + 86 371 86609669; Fax: + 86 371 86609669

E-mail address: mainzh@163.com, chunsenliu@zzuli.edu.cn or dumiao@zzuli.edu.cn

Contents

- S1 Crystal structure of as-synthesized 525-MOF**
- S2 Chemical structure and components of 525-MOF and $\text{Fe}_3\text{O}_4@\text{mC}$ nanocomposites**
- S3 Surface morphology of 525-MOF**
- S4 Nitrogen adsorption and desorption measurements**
- S5 EIS Nyquist plots and equivalent circuit**
- S6 Electrochemical performance of the aptasensors based on 525-MOF and series of $\text{Fe}_3\text{O}_4@\text{mC}$ nanocomposites**
- S7 Electrochemical performance of the aptasensors based on $\text{mFe}_3\text{O}_4@\text{mC}$ nanocomposite**
- S8 Electrochemical performance of the aptasensors based on mFe_3O_4**
- S9 Comparison of different kinds of aptasensors**
- S10 Real LOD detection**
- S11 Reproducibility and regenerability of the $\text{Fe}_3\text{O}_4@\text{mC}_{900}$ -based aptasensor**

S1 Crystal structure of as-synthesized 525-MOF

Solvothermal reaction of $\text{FeSO}_4 \cdot 7\text{H}_2\text{O}$, and 4,4',4''-nitriлотrisbenzoic acid (H_3NTB) in *N*-methyl-2-pyrrolidone (NMP) and *N*-methylformamide (NMF) produces brown plate crystals of $[\text{Fe}_{1.5}(\text{NTB})(\text{NMP})](\text{NMF})_{0.5}(\text{H}_2\text{O})$ (525-MOF). The findings were as follows: IR (KBr, cm^{-1}): 3414w (br), 1682m, 1654m, 1592vs, 1555m, 1505m, 1398vs, 1318m, 1266m, 1173m, 1102w, 1013w, 840w, 784m, 713w, 671w, 629w, 583w, 532w, 513w, and 436w were used for comparison. Single-crystal X-ray diffraction analysis indicates that 525-MOF crystallizes in the monoclinic $C2/c$ space group (**Table S1**). The asymmetric coordination unit of 525-MOF contains two crystallographic independent Fe^{2+} ions, one NTB, and two coordinated water ligands (**Fig. S1**). The Fe1 and Fe2 centers are six-coordinated to form octahedral coordination geometry. The coordination sphere of Fe1 is fulfilled by five carboxylate oxygen atoms from four NTB ligands and one oxygen atom from NMP, while Fe1 is coordinated by six carboxylate oxygen atoms from six different NTB ligands. The distances of Fe–O bonds range from 2.0068(15) to 2.1733(16) Å (**Table S2**). The angles around Fe^{3+} ions range from 80.17(7) to 180.0° (**Table S3**). The three carboxylate groups in full deprotonated NTB ligand adopt $\mu_2\text{-}\eta^1\text{:}\eta^2$, $\mu_3\text{-}\eta^1\text{:}\eta^2$ and $\mu_2\text{-}\eta^1\text{:}\eta^1$ coordination modes, respectively (**Fig. 1a**). The Fe^{2+} ions are connected by the carboxylate groups of NTB ligands to result in the 1-D rod-shaped inorganic SBU (**Fig. 1b**), which can be viewed as the edge-sharing arrangement of metal-carboxylate trinuclear units (-Fe1-Fe2-Fe1-). Each trinuclear cluster is the corner-sharing coordination polyhedrons of Fe1, Fe2, and Fe1 in a sequence of -Fe1-Fe2-Fe1-

along the *b*-axis. The Fe⋯Fe separations linked by the carboxylate groups are 3.41 Å for Fe1⋯Fe2 and 3.28 Å for Fe1⋯Fe1, respectively. Then, the adjacent rod-shaped SBUs are further linked by NTB ligands to result in a 3-D framework (**Fig. 1c**). The free void is 20.9% (1168.2 Å³ of 5586.2 Å³ per unit cell volume) calculated by PLATON (with 1.8 Å probe radius).¹

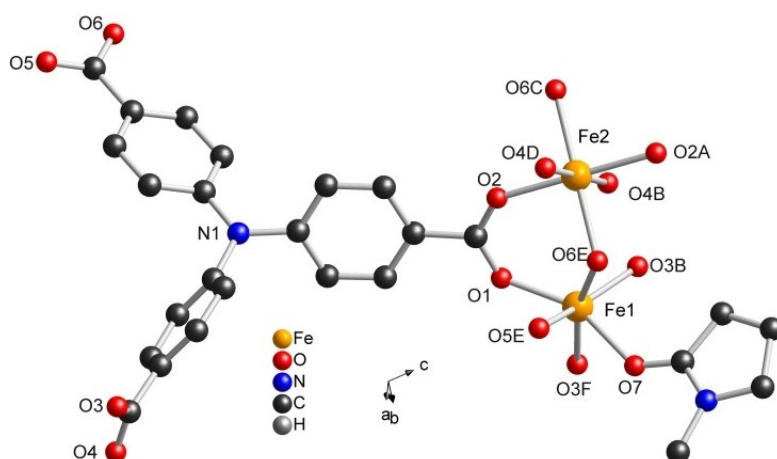


Fig. S1 Coordination environment of Fe²⁺ ions (Symmetry codes: $-x + 3/2, -y + 1/2, -z + 2$ for A; $x, -y + 1, z + 1/2$ for B; $-x + 1, y, -z + 3/2$ for C; $-x + 3/2, y - 1/2, -z + 3/2$ for D; $x + 1/2, -y + 1/2, z + 1/2$ for E; $-x + 3/2, y + 1/2, -z + 3/2$ for F).

Table S1 Crystal data and structure refinement for 525-MOF.

Compound reference	525-MOF
Chemical formula	C ₅₆ H ₅₀ Fe ₃ N ₆ O ₁₆
Formula weight	1230.57
Temperature (K)	293(2)
Crystal system	monoclinic
Space group	C2/c
a (Å)	26.7370(9)
b (Å)	8.8697(2)
c (Å)	27.0881(8)
Volume (Å ³)	5586.2(4)
Z	4
μ (mm ⁻¹)	6.800
R _{int}	0.0265
Goodness-of-fit on F ²	1.039
R ₁ ^a values [I > 2 σ (I)]	0.0360
wR ^b (F ²) values [I > 2 σ (I)]	0.0938
R ₁ ^a values (all data)	0.0407
wR ^b (F ²) values (all data)	0.0965
Completeness	100%
CCDC number	1543561

Table S2 Selected bond lengths (Å) for 525-MOF.

Atom	Atom	Length/Å
Fe2	O6 ¹	2.1451(16)
Fe2	O6 ²	2.1451(16)
Fe2	O4 ³	2.0897(16)
Fe2	O4 ⁴	2.0897(16)
Fe2	O2 ⁵	2.0888(15)
Fe2	O2	2.0887(15)
Fe1	O3 ⁶	2.1733(16)
Fe1	O3 ³	2.1280(15)
Fe1	O6 ¹	2.1194(16)
Fe1	O1	2.0068(15)
Fe1	O7	2.0814(18)

Symmetry transformations used to generate equivalent atoms. ¹ $1/2 + x, 1/2 - y, 1/2 + z$; ² $1 - x, + y, 3/2 - z$; ³ $+ x, 1 - y, 1/2 + z$; ⁴ $3/2 - x, - 1/2 + y, 3/2 - z$; ⁵ $3/2 - x, 1/2 - y, 2 - z$; ⁶ $3/2 - x, 1/2 + y, 3/2 - z$.

Table S3 Selected bond angles (°) for 525-MOF.

Atom	Atom	Atom	Angle/°	Atom	Atom	Atom	Angle/°
O6 ¹	Fe2	O6 ²	180.00(6)	O1	Fe1	O3 ⁴	109.13(7)
O4 ³	Fe2	O6 ²	89.40(6)	O1	Fe1	O3 ⁶	91.95(6)
O4 ⁴	Fe2	O6 ¹	89.40(6)	O1	Fe1	O6 ²	102.52(7)
O4 ⁴	Fe2	O6 ²	90.60(6)	O1	Fe1	O7	154.83(7)
O4 ³	Fe2	O6 ¹	90.60(6)	O7	Fe1	O3 ⁴	93.23(7)
O4 ⁴	Fe2	O4 ³	180.0	O7	Fe1	O3 ⁶	80.17(7)
O2	Fe2	O6 ¹	88.46(6)	O7	Fe1	O6 ²	85.98(7)
O2 ⁵	Fe2	O6 ¹	91.54(6)	Fe1 ⁷	O3	Fe1 ³	99.46(6)
O2	Fe2	O6 ²	91.54(6)	C14	O3	Fe1 ³	126.11(13)
O2 ⁵	Fe2	O6 ²	88.46(6)	C14	O3	Fe1 ⁷	117.99(13)
O2 ⁵	Fe2	O4 ³	90.53(7)	Fe1 ⁸	O6	Fe2 ¹	106.45(6)
O2 ⁵	Fe2	O4 ⁴	89.47(7)	C21	O6	Fe2 ¹	132.00(15)
O2	Fe2	O4 ³	89.48(7)	C21	O6	Fe1 ⁸	97.49(14)
O2	Fe2	O4 ⁴	90.52(7)	C1	O1	Fe1	128.65(15)
O2	Fe2	O2 ⁵	180.0	C14	O4	Fe2 ⁶	142.92(16)
O3 ⁴	Fe1	O3 ⁶	80.54(6)	C1	O2	Fe2	137.19(16)
O6 ²	Fe1	O3 ⁴	95.91(6)	C22	O7	Fe1	132.43(19)
O6 ²	Fe1	O3 ⁶	165.45(6)	O1	Fe1	O3 ⁴	109.13(7)

Symmetry transformations used to generate equivalent atoms. ¹ $1 - x, + y, 3/2 - z$; ²
 $1/2 + x, 1/2 - y, 1/2 + z$; ³ $3/2 - x, - 1/2 + y, 3/2 - z$; ⁴ $+ x, 1 - y, 1/2 + z$; ⁵ $3/2 - x, 1/2$
 $- y, 2 - z$; ⁶ $3/2 - x, 1/2 + y, 3/2 - z$; ⁷ $+ x, 1 - y, - 1/2 + z$; ⁸ $- 1/2 + x, 1/2 - y, - 1/2 + z$.

S2 Chemical structure and components of 525-MOF and Fe₃O₄@mC nanocomposites

The XRD patterns of 525-MOF, FeO_x@mC₃₅₀, FeO_x@mC₅₅₀, FeO_x@mC₇₀₀ and FeO_x@mC₉₀₀ (Here, x was used to represent the iron oxide due to the uncertain of the proportion of iron and oxygen) were also shown in **Figs. S2a and S2b**. The XRD pattern of 525-MOF showed well-defined diffraction peaks at $2\theta = 7.5^\circ, 13^\circ, 14.1^\circ, 20^\circ$ and 24° , and the main peaks were in agreement with that of the simulated 525-MOF (**Fig. S2a**). The diffraction peaks of FeO_x@mC₃₅₀ at $2\theta = 24^\circ, 32^\circ, 35^\circ, 41^\circ, 49^\circ, 54^\circ, 62^\circ, 64^\circ$ in all XRD patterns matched well with crystal planes of pure solid α -Fe₂O₃ (**Fig. S2b**). Both the characteristics diffraction peaks of Fe₂O₃ and Fe₃O₄ were simultaneously observed on the XRD patterns of FeO_x@mC₅₅₀ (**Fig. S2b**). During the thermal decomposition process, the relatively high temperature induced the conversion of Fe₂O₃ into Fe₃O₄. As for FeO_x@mC₇₀₀ and FeO_x@mC₉₀₀ (**Fig. S2b**), the characteristic diffraction peaks at $30^\circ, 36^\circ, 43^\circ, 54^\circ, 57^\circ$, and 63° were indexed as the diffractions of the (220), (311), (400), (422), (511), and (440) crystalline planes of Fe₃O₄ according to the standard spectrum of magnetite and no other crystalline planes were found in the XRD pattern (JCPDS card no. 19-629).

The progress of 525-MOF calcined to prepare Fe₃O₄@mC nanocomposites was followed by thermo-gravimetric analysis (TGA) curve as shown in **Fig. S2c**. The first mass loss stage (ca. 22%) from 180 °C to 350 °C was due to the volatilization of the solvent (NMP and NMF) accompanied by breakdown of formic acid. The drastic mass loss (ca. 20%) from 450 °C to 500 °C, slow mass loss (ca. 2%) from 500 °C to

590 °C and another mass loss (ca. 14%) from 590 °C to 650 °C were observed and the XRD characterization indicated that the conversion from Fe_2O_3 to Fe_3O_4 occurred at these three stages (discussed above). The conversion could be attributed to the incomplete calcined products as evidenced by thermal stability. The phase corresponding to the $\text{Fe}_3\text{O}_4@m\text{C}$ nanocomposites was stabilized at 650 °C. After 650 °C, the 525-MOF were nearly decomposed thus almost unchanged mass loss was observed. The carbon generated during the calcination which has been proven in XPS full-spectra of $\text{Fe}_3\text{O}_4@m\text{C}$ nanocomposites (Fig. S3) could act as a buffer to prevent aggregation of metal oxides.

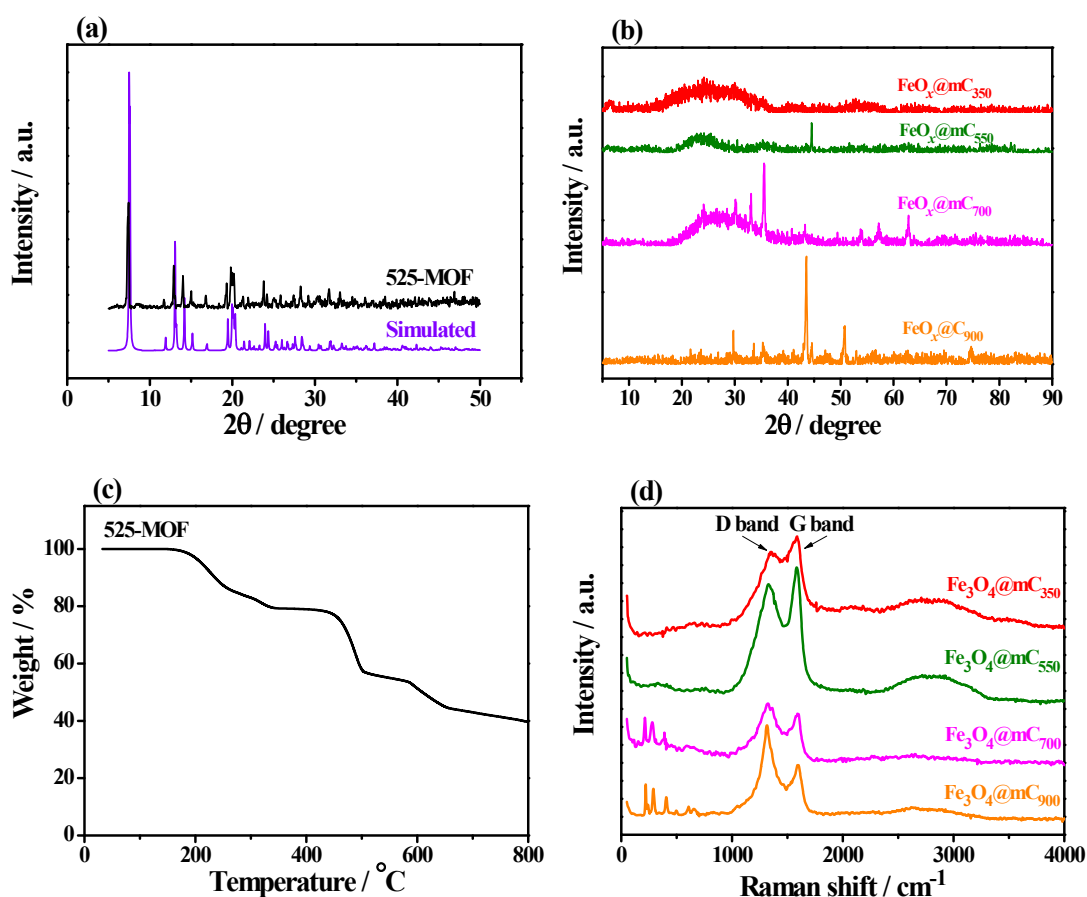


Fig. S2 (a) XRD and (c) TGA of 525-MOF; (b) XRD and (d) Raman of $\text{Fe}_3\text{O}_4@m\text{C}$ nanocomposites.

Table S4 Raman data for different Fe₃O₄@mC nanocomposites.

Samples	Raman data
	<i>I_D/I_G</i>
Fe ₃ O ₄ @mC ₃₅₀	0.89
Fe ₃ O ₄ @mC ₅₅₀	0.91
Fe ₃ O ₄ @mC ₇₀₀	1.02
Fe ₃ O ₄ @mC ₉₀₀	1.57

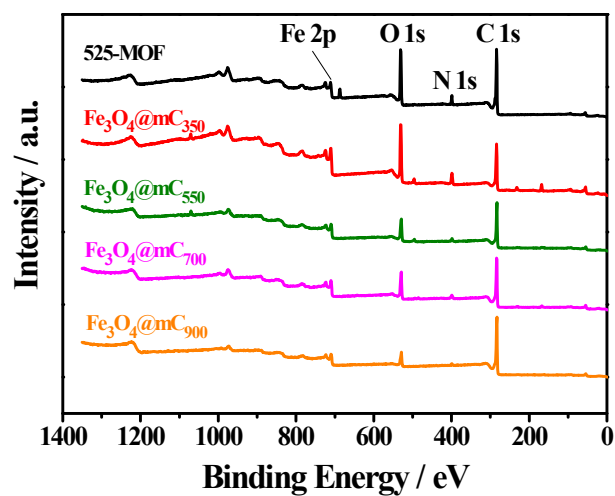


Fig. S3 Full XPS spectra of 525-MOF, $\text{Fe}_3\text{O}_4@\text{mC}_{350}$, $\text{Fe}_3\text{O}_4@\text{mC}_{550}$, $\text{Fe}_3\text{O}_4@\text{mC}_{700}$, and $\text{Fe}_3\text{O}_4@\text{mC}_{900}$ nanocomposites.

Table S5 The atomic% of the 525-MOF and different $\text{Fe}_3\text{O}_4@\text{mC}$ nanocomposites before and after pyrolysis.

Samples	Atomic%			
	C 1s	Fe 2p	N 1s	O 1s
525-MOF	67.86	4.70	5.16	22.27
$\text{Fe}_3\text{O}_4@\text{mC}_{350}$	55.10	5.18	9.85	29.87
$\text{Fe}_3\text{O}_4@\text{mC}_{550}$	70.64	4.90	3.61	20.85
$\text{Fe}_3\text{O}_4@\text{mC}_{700}$	72.68	4.23	4.62	18.47
$\text{Fe}_3\text{O}_4@\text{mC}_{900}$	83.20	3.19	2.68	10.94

S3 Surface morphology of 525-MOF

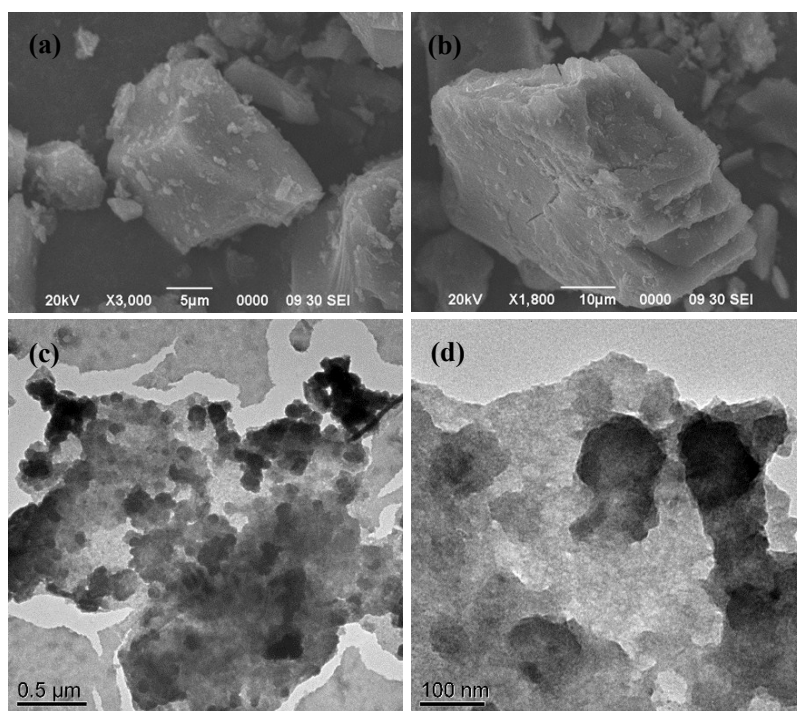


Fig. S4 Low- and high-magnitude (a, b) SEM and (c, d) TEM images of 525-MOF.

S4 Nitrogen adsorption and desorption measurements

The nitrogen adsorption and desorption isotherms of different Fe₃O₄@mC nanocomposites are shown in **Figs. S5a1, b1, c1, and d1**. After 525-MOF were pyrolyzed under different temperatures, the type IV isotherms of Fe₃O₄@mC₃₅₀, Fe₃O₄@mC₅₅₀, Fe₃O₄@mC₇₀₀, and Fe₃O₄@mC₉₀₀ display the presence of mesopores on the different Fe₃O₄@mC nanocomposites. The N₂ uptakes for the four pyrolyzed products around 1 atm at 77 K are 19.29, 85.19, 154.71 and 202.82 cm³·g⁻¹, respectively, and the Brunauer–Emmett–Teller (BET) specific areas are calculated to be 27.24, 123.81, 204.55 and 258.03 m²·g⁻¹ for Fe₃O₄@mC₃₅₀, Fe₃O₄@mC₅₅₀, Fe₃O₄@mC₇₀₀, and Fe₃O₄@mC₉₀₀, respectively. While for the pore size distribution obtained from the Barrett–Joyner–Halenda (BJH) method (**Figs. S5a2, b2, c2, and d2**), Fe₃O₄@mC₃₅₀ revealed two narrow distributions centered at 3–5 and 6–14 nm; Fe₃O₄@mC₅₅₀ revealed a narrow distribution centered at 3–5 nm and a wide distribution centered at 6–11 nm; Fe₃O₄@mC₇₀₀ revealed a narrow distribution centered at 3–5 nm and a wide distribution centered at 6–17 nm; Fe₃O₄@mC₉₀₀ revealed a narrow distribution centered at 3–5 nm and a wide distribution centered at 6–17 nm. The pore size distribution clearly reveals that the majority of pores are in the mesoporous region, and the nitrogen adsorption by the mesopores is much higher than that of micropores.

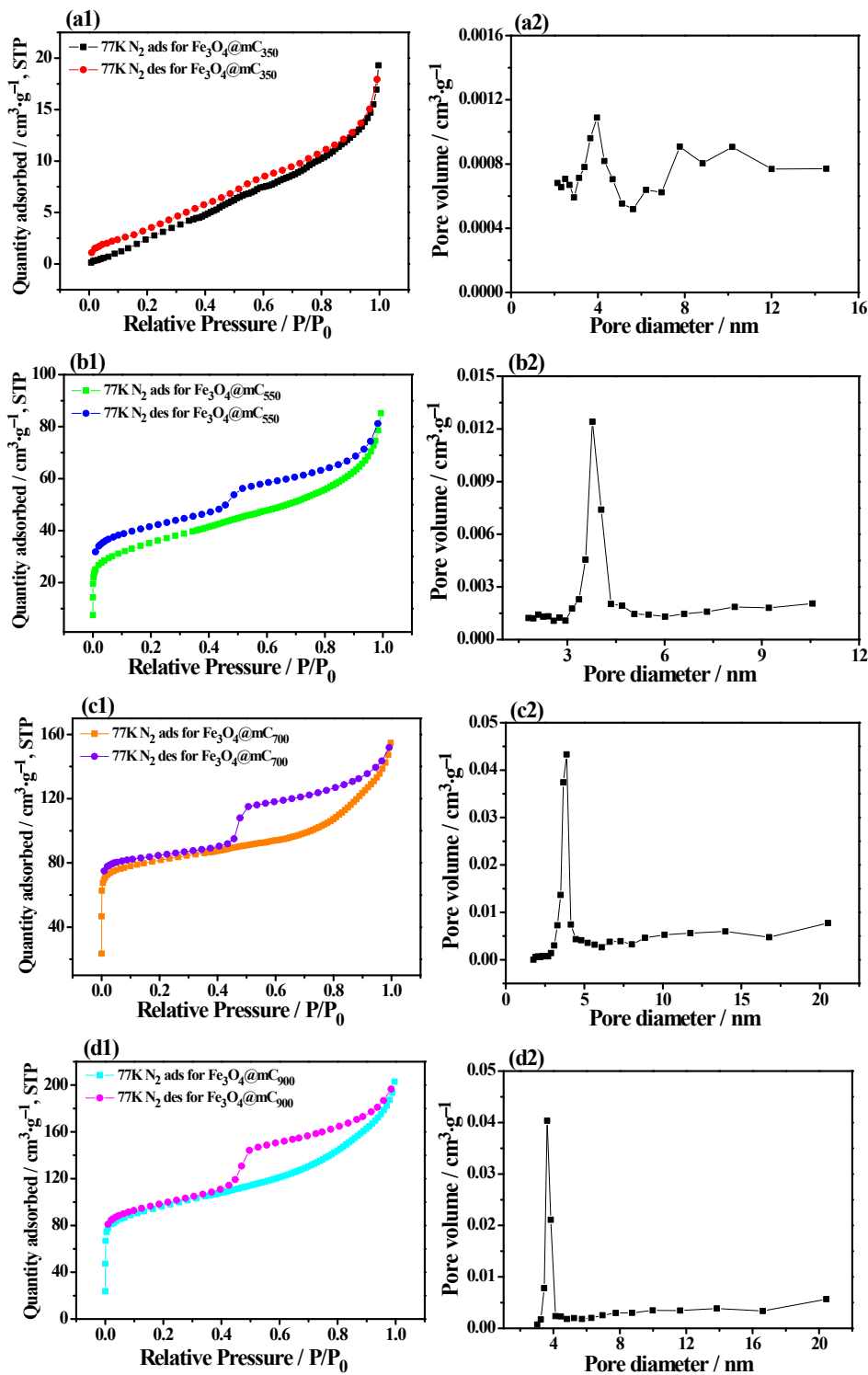


Fig. S5 (a1, b1, c1, and d1) Nitrogen adsorption–desorption isotherms and (a2, b2, c2, and d2) Pore size distributions of (a) $\text{Fe}_3\text{O}_4@m\text{C}_{350}$, (b) $\text{Fe}_3\text{O}_4@m\text{C}_{550}$, (c) $\text{Fe}_3\text{O}_4@m\text{C}_{700}$, and (d) $\text{Fe}_3\text{O}_4@m\text{C}_{900}$ nanocomposites obtained from the BJH method.

For comparison, we also used the Nonlocal Density Functional Theory (NLDFT) method to estimate the pore size distribution, and the corresponding plots are shown in **Fig. S6**. It can be obviously observed that, the four nanocomposites all reveal a wide distribution in the range of approximately 3–20 nm. However, the distribution plots are dispersive and heterogeneous, and cannot obey the Gaussian distribution, therefore, the BJH method is much more appropriate for the estimation of the as-prepared $\text{Fe}_3\text{O}_4@\text{mC}$ nanocomposites than NLDFT method.

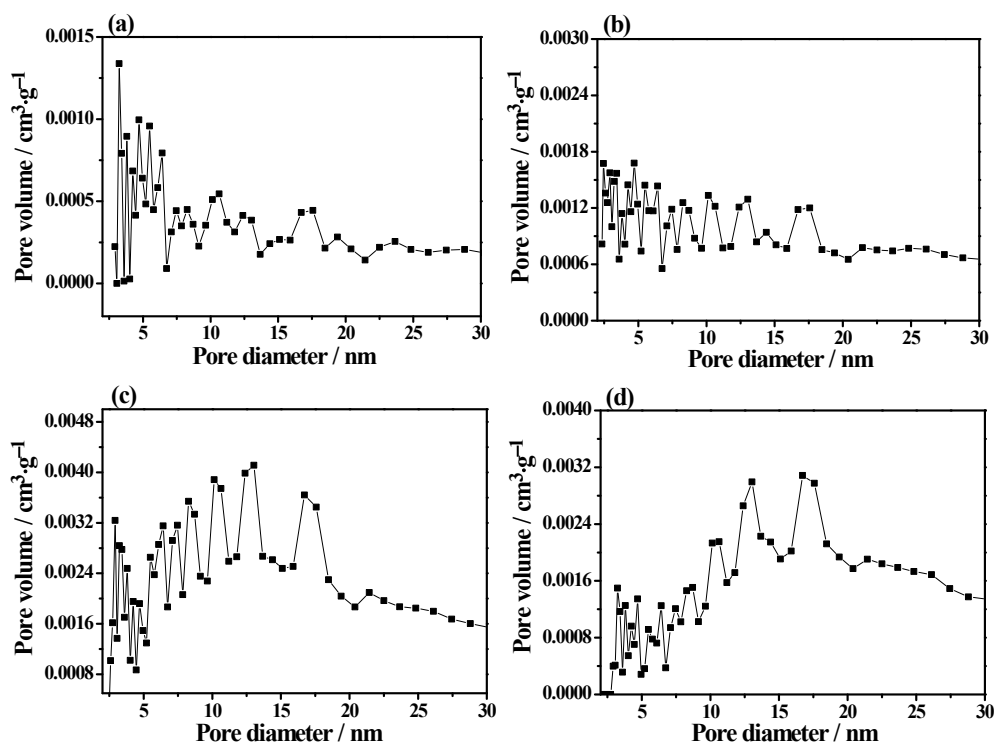


Fig. S6 Pore size distributions of (a) $\text{Fe}_3\text{O}_4@\text{mC}_{350}$, (b) $\text{Fe}_3\text{O}_4@\text{mC}_{550}$, (c) $\text{Fe}_3\text{O}_4@\text{mC}_{700}$, and (d) $\text{Fe}_3\text{O}_4@\text{mC}_{900}$ nanocomposites obtained from the NLDFT method.

S5 EIS Nyquist plots and equivalent circuit

The EIS spectra were analyzed using Zview2 software. A nonlinear least-squares method was used to fit and determine the parameters of the elements in an equivalent circuit (Fig. S7). The Randles equivalent circuit, which consists of solution resistance (R_s), charge-transfer resistance (R_{ct}), constant-phase element (CPE), and Warburg impedance (W_o), was shown in the inset of Fig. S7.

As shown in the typical EIS spectrum (Fig. S7), the Z' (real part) versus Z'' (imaginary part) means that the electron-transfer resistance (R_{ct}) at the electrode surface was the same as the diameter of the semicircle on the Nyquist plot and can be used to describe the properties at the interface between the electrode and analyte solution.² The Nyquist plot is composed of two sections: the semicircle part at higher frequencies belonging to the electron-transfer limited process and the linear portion at lower frequency range corresponding to the diffusion-limited process.

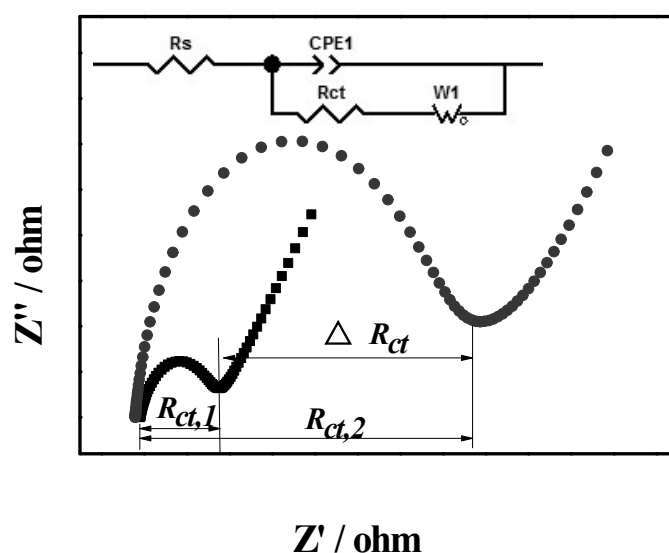


Fig. S7 The typical EIS Nyquist plot and equivalent circuit.

S6 Electrochemical performance of the aptasensors based on 525-MOF and series of Fe₃O₄@mC nanocomposites

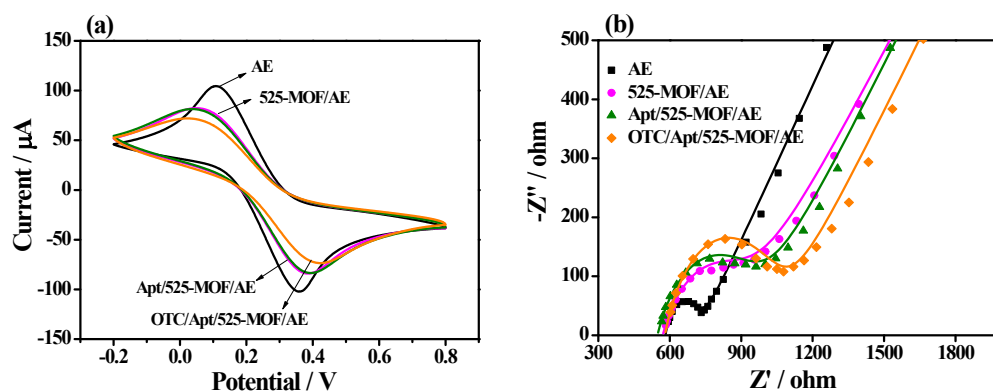


Fig. S8 (a) CV curves and (b) EIS plots to trace the whole procedure of the OTC detection using the developed aptasensor based on 525-MOF in 5 mM $[\text{Fe}(\text{CN})_6]^{3-/4-}$ containing 0.14 M NaCl and 0.1 M KCl: AE, 525-MOF/AE, Apt/525-MOF/AE, and OTC/Apt/525-MOF/AE.

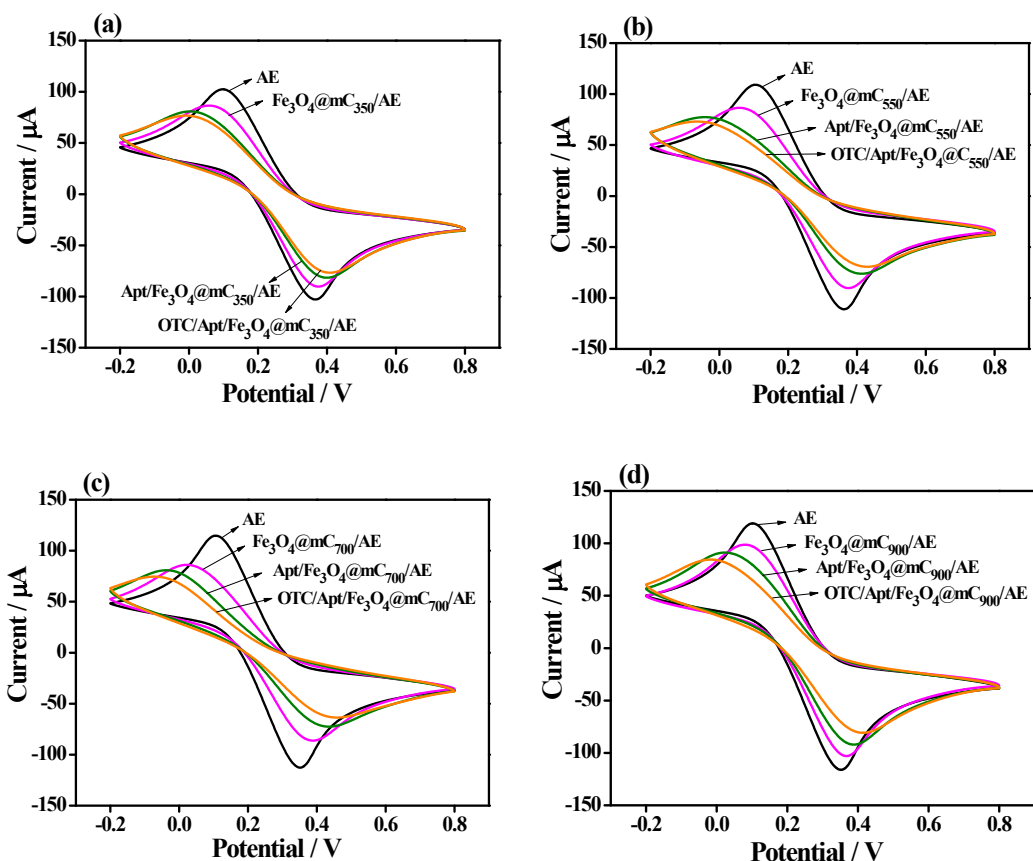


Fig. S9 CV curves to trace the whole procedure of the OTC detection using the developed aptasensor based on (a) $\text{Fe}_3\text{O}_4@\text{mC}_{350}$, (b) $\text{Fe}_3\text{O}_4@\text{mC}_{550}$, (c) $\text{Fe}_3\text{O}_4@\text{mC}_{700}$, and (d) $\text{Fe}_3\text{O}_4@\text{mC}_{900}$, respectively, in 5 mM $[\text{Fe}(\text{CN})_6]^{3-/4-}$ containing 0.14 M NaCl and 0.1 M KCl: (a) AE, $\text{Fe}_3\text{O}_4@\text{mC}_{350}/\text{AE}$, $\text{Apt}/\text{Fe}_3\text{O}_4@\text{mC}_{350}/\text{AE}$, $\text{OTC}/\text{Apt}/\text{Fe}_3\text{O}_4@\text{mC}_{350}/\text{AE}$; (b) AE, $\text{Fe}_3\text{O}_4@\text{mC}_{550}/\text{AE}$, $\text{Apt}/\text{Fe}_3\text{O}_4@\text{mC}_{550}/\text{AE}$, $\text{OTC}/\text{Apt}/\text{Fe}_3\text{O}_4@\text{mC}_{550}/\text{AE}$; (c) AE, $\text{Fe}_3\text{O}_4@\text{mC}_{700}/\text{AE}$, $\text{Apt}/\text{Fe}_3\text{O}_4@\text{mC}_{700}/\text{AE}$, $\text{OTC}/\text{Apt}/\text{Fe}_3\text{O}_4@\text{mC}_{700}/\text{AE}$; and (d) AE, $\text{Fe}_3\text{O}_4@\text{mC}_{900}/\text{AE}$, $\text{Apt}/\text{Fe}_3\text{O}_4@\text{mC}_{900}/\text{AE}$, $\text{OTC}/\text{Apt}/\text{Fe}_3\text{O}_4@\text{mC}_{900}/\text{AE}$.

S7 Electrochemical performance of the aptasensors based on the mFe₃O₄@mC nanocomposite

As reported previously, the Fe₃O₄ and mesoporous carbon are combined and formed the mFe₃O₄@mC nanocomposite and exhibited core-shell and sphere-like structure with mesoporous morphology simultaneously.³ It is quite different from the Fe₃O₄@mC derived from 525-MOF, of which the Fe₃O₄ and mesoporous carbon show their individual structure. Consequently, it leads to the substantial different electrochemical sensing performance of the two nanocomposites. Herein, the mFe₃O₄@mC-based aptasensor for detecting OTC was fabricated and investigated using CV and EIS. As for the CV measurements (**Fig. S10a**), the ΔE_p values for AE, mFe₃O₄@mC/AE, Apt/mFe₃O₄@mC/AE, and OTC/Apt/mFe₃O₄@mC/AE are 254, 270, 317, and 386 mV, while the R_{ct} values of the four modified AEs for mFe₃O₄@mC are 68.52, 352.3, 447.4, and 574.9 Ω (**Fig. S10b**). Besides, the ΔR_{ct} values of each step for mFe₃O₄@mC-based aptasensor are 283.78, 95.1, and 127.5 Ω , respectively (**Fig. S13**). All of these results suggest that the mFe₃O₄@mC-based aptasensor also can be used to sensitively detect OTC.

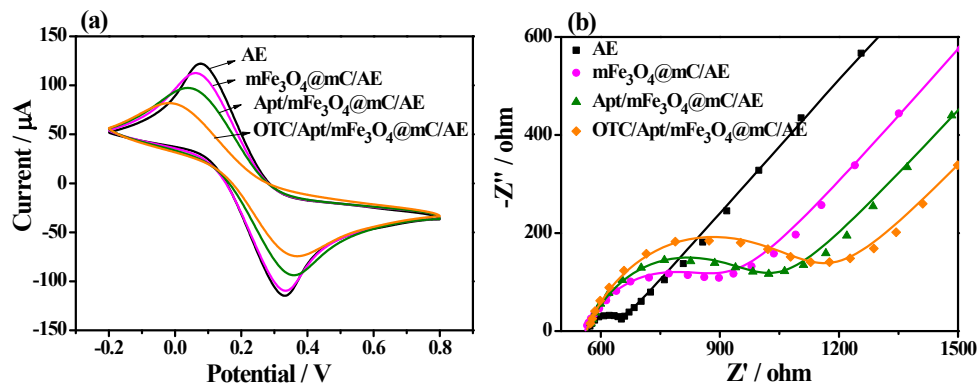


Fig. S10 (a) CV curves and (b) EIS plots to trace the whole procedure of the OTC detection using the developed aptasensor based on mFe₃O₄@mC in 5 mM [Fe(CN)₆]^{3-/4-} containing 0.14 M NaCl and 0.1 M KCl: AE, mFe₃O₄@mC/AE, Apt/mFe₃O₄@mC/AE, OTC/Apt/mFe₃O₄@mC/AE.

S8 Electrochemical performance of the aptasensors based on mFe₃O₄

In order to verify the role of mesoporous carbon in sensing OTC, a new mesoporous iron oxide without mesoporous carbon (denoted as mFe₃O₄) was prepared using the literature method.⁴ Subsequently, the as-prepared mFe₃O₄ was used to construct the mFe₃O₄-based aptasensor for detecting OTC, and the electrochemical performance was investigated using CV and EIS. As for the CV measurements (**Fig. S11a**), the ΔE_p values for AE, mFe₃O₄/AE, Apt/mFe₃O₄/AE, and OTC/Apt/mFe₃O₄/AE are 236, 289, 338, and 350 mV, while the R_{ct} values of the four modified AEs for mFe₃O₄ are 62.0, 209.7, 390.8, and 464.8 Ω (**Fig. S11b**). Besides, the ΔR_{ct} values of each step for mFe₃O₄-based aptasensor are 147.7, 181.1, and 74.0 Ω , respectively (**Fig. S12**). By comparison with the electrochemical responses obtained at Fe₃O₄@mC₉₀₀-based aptasensor, it is obvious that, the ΔR_{ct} ($R_{ct, \text{material}} - R_{ct, \text{AE}}$) of mFe₃O₄ is much higher than that of Fe₃O₄@mC₉₀₀, suggesting the poorer conductivity of mFe₃O₄ compared with Fe₃O₄@mC₉₀₀. While the ΔR_{ct} ($R_{ct, \text{Apt}} - R_{ct, \text{material}}$) of mFe₃O₄ is much lower than that of Fe₃O₄@mC₉₀₀, indicating that the adsorption quantity of aptamer on the surface of mFe₃O₄ is lower than Fe₃O₄@mC₉₀₀, therefore leading to the lower detection efficiency for the target OTC. The main reason for this phenomenon is probably that, on one hand, the mesoporous carbon contained in Fe₃O₄@mC₉₀₀ possesses good conductivity and benefits for the Fe₃O₄@mC₉₀₀/AE to transfer electron with the electrolyte; on the other hand, the functional groups (such as C–N, C–O, and COO–) existed in the mesoporous carbon in Fe₃O₄@mC₉₀₀ can form covalent attachment with aptamer strands and provide favorable environments for

aptamer immobilization, and therefore facilitates the detection of target OTC.

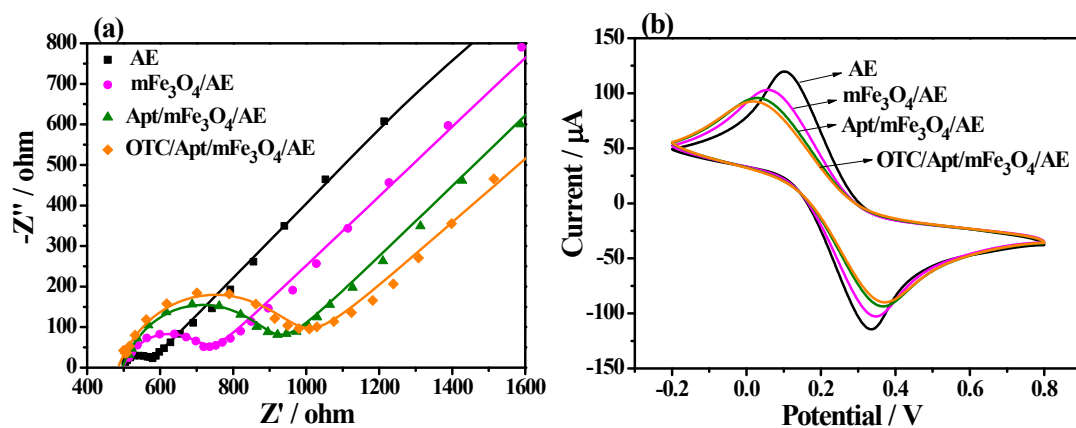


Fig. S11 (a) CV curves and (b) EIS plots to trace the whole procedure of the OTC detection using the developed aptasensor based on $m\text{Fe}_3\text{O}_4$ in 5 mM $[\text{Fe}(\text{CN})_6]^{3-/4-}$ containing 0.14 M NaCl and 0.1 M KCl: AE, $m\text{Fe}_3\text{O}_4/\text{AE}$, Apt/ $m\text{Fe}_3\text{O}_4/\text{AE}$, OTC/Apt/ $m\text{Fe}_3\text{O}_4/\text{AE}$.

S9 Comparison of different kinds of aptasensors

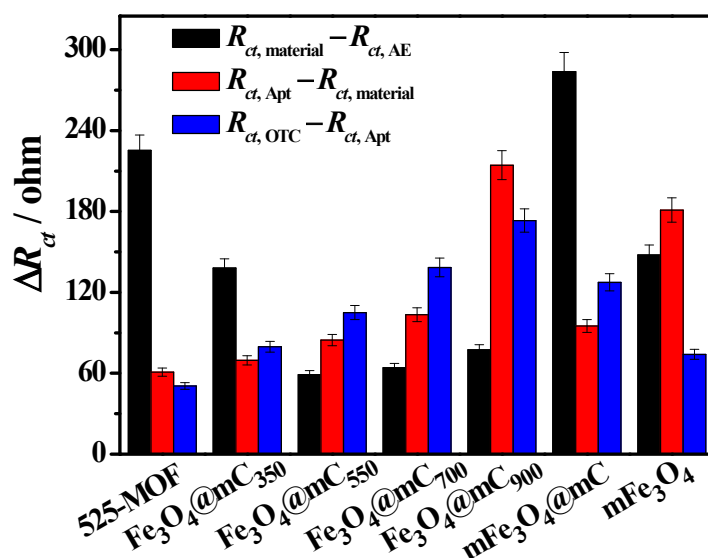


Fig. S12 Differences in ΔR_{ct} values at each stage for the OTC detection using the developed aptasensors based on 525-MOF, $\text{Fe}_3\text{O}_4@m\text{C}_{350}$, $\text{Fe}_3\text{O}_4@m\text{C}_{550}$, $\text{Fe}_3\text{O}_4@m\text{C}_{700}$, $\text{Fe}_3\text{O}_4@m\text{C}_{900}$, $m\text{Fe}_3\text{O}_4@m\text{C}$ nanocomposites, and $m\text{Fe}_3\text{O}_4$.

S10 Real LOD detection

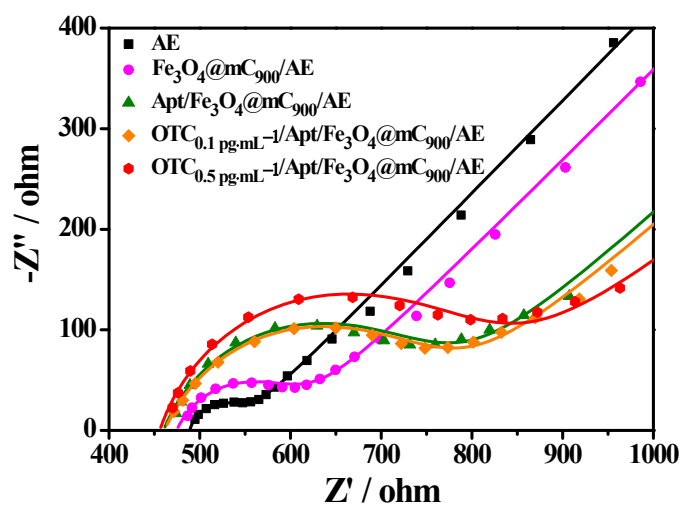


Fig. S13 EIS plots to trace the R_{ct} variation using Fe₃O₄@mC₉₀₀-aptasensor to detect 0.1 and 0.5 pg·mL⁻¹ of OTC.

S11 Reproducibility and regenerability of the Fe₃O₄@mC₉₀₀-based aptasensor

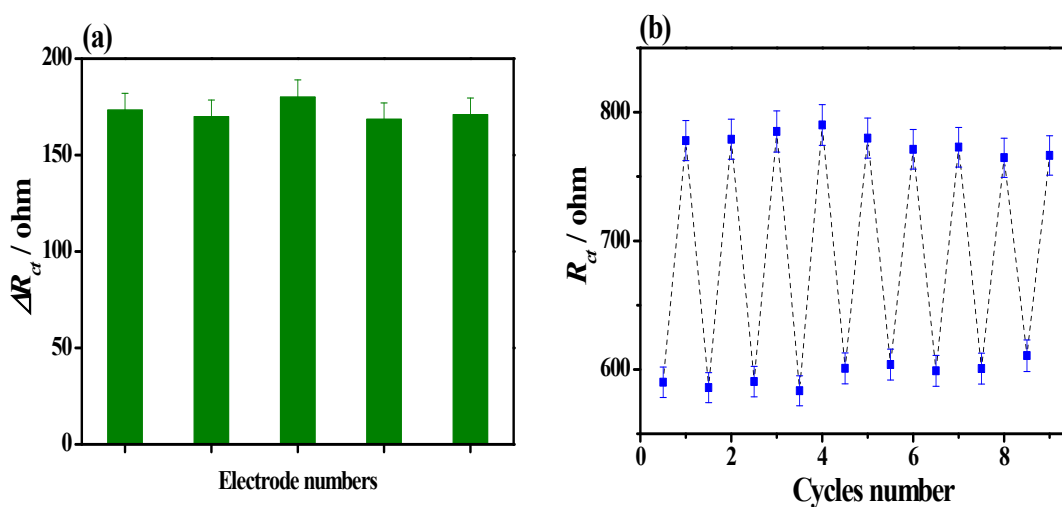


Fig. S14 (a) Reproducibility and (b) regenerability of the Fe₃O₄@mC₉₀₀-based aptasensor for detecting OTC with the concentration of 0.005 ng·mL⁻¹.

References

- [1] A. L. Spek, *J. Appl. Crystallogr.*, 2003, **36**, 7–13.
- [2] W. Wang, L. Wang, L. Zou, G. Li and B. Ye, *J. Electroanal. Chem.*, 2016, **772**, 17–26.
- [3] Z. Zhang, H. Ji, Y. Song, S. Zhang, M. Wang, C. Jia, J.-Y. Tian, L. He, X. Zhang and C.-S. Liu, *Biosens. Bioelectron.*, 2017, **94**, 358–364.
- [4] K. Gandha, J. Mohapatra, M. K. Hossain, K. Elkins, N. Poudyal, K. Rajeshwar and J. P. Liu, *RSC Adv.*, 2016, **6**, 90537–90546.